Acta Geologica Polonica, Vol. 72 (2022), No. 3, pp. 353–368
DOI: 10.24425/agp.2022.140430

A multi-analytical approach for the analysis of cation distribution in a aluminoceladonite structure

MARIOLA KĄDZIOŁKA-GAWEŁ[1], MATEUSZ DULSKI[2], MARIA CZAJA[3], TOMASZ KRZYKAWSKI[3] and MAGDALENA SZUBKA[1]

[1] *Institute of Physics, University of Silesia, 75 Pułku Piechoty 1, 41-500 Chorzów, Poland; e-mails: mariola.kadziolka-gawel@us.edu.pl; magdalena.szubka@us.edu.pl*
[2] *Institute of Material Science, University of Silesia, 75 Pułku Piechoty 1a, 41-500 Chorzów, Poland; e-mail: mateusz.dulski@us.edu.pl*
[3] *Faculty of Earth Sciences, University of Silesia, Będzińska 60, 41-200 Sosnowiec, Poland; e-mails: tomasz.krzykawski@us.edu.pl; maria.czaja@us.edu.pl*

ABSTRACT:

Kądziołka-Gaweł, M., Dulski, M., Czaja, M., Krzykawski, T. and Szubka, M. 2022. A multi-analytical approach for the analysis of cation distribution in a aluminoceladonite structure. *Acta Geologica Polonica*, **72** (3), 353–368. Warszawa.

In this paper cation arrangement in two samples of aluminoceladonite, emerald-green and dark-green were studied by Mössbauer, Raman and X-ray photoelectron spectroscopies. The X-ray photoelectron spectroscopy (XPS) spectra obtained in the region of the Si2p, Al2p, Fe2p, K2p, and O1s core levels provided information, for the first time highlighting a route to identify the position of Si, Al, K, and Fe cations in a structure of layered silicates. The XPS analysis showed the presence of Al in tetrahedral and octahedral coordination while the K2p line indicated the possibility of K^+ substitution by other cations in interlayer sites. Mössbauer spectroscopy provided information about crystal chemistry with respect to the local electronic and geometric environment around the Fe atom and to distortions of the polyhedra. It turned out that iron was located mostly in the *cis*-octahedra position wherein about 75% of iron appeared in the form of Fe^{3+}. The most preferred cation combinations around Fe corresponded to $3Fe^{3+}$ ions and $MgFe^{2+}Fe^{3+}/2MgFe^{3+}$. Raman spectroscopy illustrated aluminium substitution in silicon and iron positions wherein the concentration of the aluminium determined the degree of structural distortion within the layered system. These isomorphic substitutions implied a typical band arrangement in the hydroxyl region, which has not been observed in celadonites so far.

Key words: Aluminoceladonite; Ions position characterization isomorphic substitutions; Fe-bearing phyllosilicates; X-ray photoelectron spectroscopy; Mössbauer spectroscopy; Raman spectroscopy.

INTRODUCTION

There has been a great interest in the mineralogy, crystallography and potential novel technological applications of layer silicates for many decades (Foster 1960; Li *et al.* 1997; Elmi *et al.* 2014). Dioctahedral phyllosilicates are formed as two tetrahedral sheets based on interconnected six-membered rings of SiO_4^{-4}. Three out of the four oxygens from each tetrahedron are shared with other tetrahedra. The apical oxygens and the OH ions are bonded to Me^{2+} or Me^{3+} cations in octahedral coordination. Two tetrahedral sheets with an octahedral one between them form a unit called layer 2:1 (Drits *et al.* 2006; Zviagina *et al.* 2007). The unit cell contains three symmetrically independent octahedra, one *trans*- (M1) and

two *cis*-octahedra (M2), differing in the positions of OH groups. Adjacent *cis*-octahedra share an edge formed by two OH groups whereas in *trans*-octahedra hydroxyls are located opposite to each other. The wide variety of isomorphous cation substitutions in octahedra (i.a. Fe^{3+}, Fe^{2+}, Mg, Al) and tetrahedra (Si, Al) (Richardson and Richardson 1982; Tischendorf *et al*. 2007) are characteristic of 2:1 layer silicates. The accurate crystal-chemical description of these minerals is often a challenge because of: the presence of the same element in different structural sites, long- and short-range ordering of cation distribution or homo- and heterovalent substitutions, which are widespread and modify their properties (Tsipursky and Drits 1984; Brigatti *et al.* 1998; Drits *et al.* 2006; Muller *et al.* 2000). Determination of cation arrangement in a dioctahedral layered silicate is a complex problem and even diffraction methods yield data only on the averaged composition of cations in the unit-cell sites, ignoring a possible short-range ordering. The knowledge of cation arrangement is important for evaluating the overall energy and stability of these structures and powder XRD can provide only an average occupancy of sites.

To obtain more local information, Mössbauer spectroscopy of iron has become an established method in investigation of minerals, including phyllosilicates (HellerKallai and Rozenson 1981; DeGrave 1987; Dainyak *et al*. 2006). A typical Mössbauer spectrum of silicate is composed of doublets, each corresponding to Fe in a distinct site or valence state. Isomer shift (IS) and quadrupole splitting (QS) are fundamental parameters that describe the positions of two doublet peaks. Mössbauer spectroscopy gives information about oxidation states and coordination numbers, which are identified on the basis of the magnitudes of the isomer shifts and quadrupole splitting. Site symmetries are also characterized by the quadrupole splitting, and the magnitudes of this parameter have often been used to distinguish different sites with the same coordination number. Additionally, the crystal-chemical models (Tsipursky and Drits 1984; Dainyak *et al.* 2004, 2006; Zviagina *et al.* 2015) have shown that the QS parameter allows to determine the local cation arrangement of Fe^{3+} and Fe^{2+}.

Raman and infrared spectroscopies also provide the possibility of identifying the type of mica-minerals due to the correlation between crystal structure and characteristic band arrangement. Examination of the spectra and an explanation of the structural models of the minerals provide a basis for understanding most of the constituent units of clay minerals (Tlili *et al.* 1989; Schroeder and Far 1990; Ospitali *et al.* 2008). These units include hydroxyl groups, tetrahedral silicate/aluminate anions, octahedral metal cations, and interlayer cations. Band positions in particular regions are strongly affected by the type of cations occupying the octahedra position (Mg, Al, and Fe) (Besson and Drits 1997a, 1997b; Gates 2008; Bishop *et al.* 2017).

X-ray photoelectron spectroscopy (XPS) is a surface-sensitive technique, which determines the concentration and chemical states of elements in the very near-surface layer (1–10 nm) of both conductive and non-conductive materials (Elmi *et al*. 2016). The resulting energy spectrum has sharp peaks corresponding to the electronic energy states of the sample. The effects of chemical changes on the photoelectron peak shape have been of particular interest due to the information that may be obtained. This includes qualitative elemental analysis as well as the oxidation state and coordination environment of an element. Core binding energies for Fe, Mg, Al, Si, and O electrons in ten well-characterized silicate minerals were determined prior (Liu and Brown 1998; Elmi *et al.* 2014, 2016). XPS is a method used in mineralogy and related geoscience fields to study, for instance, the surface morphology (Kaky *et al*. 2019; MarcoBrown *et al*. 2019) or to qualitative elemental analysis (Süzer *et al*. 1999; Ihekweme *et al*. 2020) but still not use to examine crystal chemical variations like cation distribution or replacement. Even though the XPS method is generally treated as a surface sensitivity method, we think that such surface analysis of clay minerals is indeed representative of the overall bulk composition. This is to be expected since clay mineral layers should be of similar composition whether at the surface or in the center of an aggregate.

The aim of the present work was to make another attempt to combine and relate the results of different spectroscopic techniques for the analysis of the cation distribution of two Fe bearing dioctahedral mica. The results of individual Mössbauer, Raman or X-ray photoelectron spectroscopy yield a lot of answers. However, a combination of all of these techniques provides complementary outcomes in studies of phyllosilicates. The obtained results create new possibilities to find out more about cation distribution in structures of layer silicates and show that X-ray photoelectron spectroscopy can be used as a new tool to visualize cation arrangement.

MATERIALS

Several secondary minerals have been found in the altered volcanic rocks of intermediate to ba-

saltic composition in Lubiechowa near Świerzawa (Sudety Mts, Poland) from which two types of clay minerals were collected from amygdales, one emerald-green, the other of dark green. These samples look like celadonite which is found in many locations. Several types of measurements were performed for the studied samples. All measurements, except for microprobe analyses, were performed on powdered samples.

EXPERIMENTAL METHODS

Microprobe analyses

Microprobe analyses of the specimens were carried out at the Inter-Institutional Laboratory of Microanalyses of Minerals and Synthetic Substances in Warsaw, with the aid of a CAMECA SX-100 electron microprobe. Selected parts of the studied samples were embedded in resin and smoothed. Reference materials, analytical lines, diffracting crystals, mean detection limits (in wt. %) and uncertainties were as follows: rutile – Ti (Kα, PET, 0.03, 0.05), diopside – Si (Kα, TAP, 0.02, 0.21), Ca – (Kα, PET, 0.03, 0.16), orthoclase – Al (Kα, TAP, 0.02, 0.08), and K (Kα, PET, 0.03, 0.02), albite – Na (Kα, TAP, 0.01, 0.08), hematite – Fe (Kα, LIF, 0.09, 0.47), rhodochrosite – Mn (Kα, LIF, 0.03, 0.10), phlogopite – F (Kα, TAP, 0.04, 0.32), tugtupite – Cl (Kα, PET, 0.02, 0.04), Cr_2O_3 – Cr (Kα, PET, 0.04, 0.01). Results presented in Table 1 are average values from 12 measuring points.

wt. %	AlCel 1	AlCel 2
SiO_2	56.24(42)	58.58(66)
Al_2O_3	15.24(45)	9.36(39)
MgO	5.51(37)	5.82(37)
FeO_{tot}	10.90(29)	12.37(56)
FeO^*	3.22(11)	2.39(12)
$Fe_2O_3^*$	8.54(15)	11.10(57)
TiO_2	0.02(1)	0.05(2)
MnO	0.03(1)	0.01(1)
Cr_2O_3	0.06(2)	0.07(3)
K_2O	7.42(11)	8.92(49)
Na_2O	<0.01	<0.01
BaO	<0.01	<0.01
CaO	0.57(2)	0.22(12)
F	0.09(7)	0.22(12)
Cl	<0.01	<0.01
Total	96.118	95.634

Table 1. The chemical composition (wt.%) of the studied aluminoceladonite samples.* FeO and Fe_2O_3 contents were determined from the Fe^{3+}/Fe^{2+} ratios obtained from Mössbauer spectra.

X-ray diffraction

X-ray diffraction measurements were performed by CuKα radiation using a PANalytical, X'Pert Pro Multi-Purpose Diffractometer, powered by a Philips PW3040/60 X-ray generator. Data were collected in the range from 4°2θ to 90°2θ with a step size of 0.01°2θ and nominal time per step of 300 sec, with the aid of the scanning X'Celerator detector (with the active length of 2.12 °2θ). X-rays were generated from a Cu anode supplied with 40 kV voltage and a current of 40 mA. Phase identification was carried out by means of the PANalytical High Score Plus program (version 4.8) coupled with the ICDD PDF4+ (version 2018) database. Unit cell parameters refinement was performed by Rietveld semi-automatic mode for the bulk powder of both samples.

^{57}Fe Mössbauer spectroscopy

^{57}Fe Mössbauer transmission spectra were recorded at room temperature with an MS96 Mössbauer spectrometer and a linear arrangement of a ^{57}Co:Rh source, a multichannel analyzer with 1024 channels (before folding), an absorber and a detector. The samples were gently pulverized in an agate mortar under acetone and mounted with the thickness of 7 mg/cm^2 of the sample in the holder. Such an amount of the sample is optimal to reduce absorber thickness effects (Dyar 1984, 2002; Rancourt *et al.* 1992). The spectrometer was calibrated at room temperature with a 30 μm thick α-Fe foil. Numerical analysis of the Mössbauer spectra was performed by means of the MossWinn program. They were analysed with two procedure: distribution of the quadrupole splitting (QSD) and superposition of six discrete, Lorentzian-shaped, quadrupole doublets. In the QSD two distributions of QS with different isomer shifts were assumed, the first corresponding to Fe^{2+} and the second to Fe^{3+}. Each discrete point in the derived QS distribution is equivalent to a separate subspectrum (doublet) with different values of the distribution parameter (QS) and with areas weighted according to the distribution curve. The theory behind these kind of distributions is described in the paper of Hesse and Rübartsch (Hesse and Rübartsch 1974). The quadrupole splitting distribution can help find the most probable configurations at which the iron can exist in the investigated samples. The peaks of the distribution curve can then be assigned to different microenvironments, helping to give a better explanation for the Mössbauer spectra.

X-ray photoelectron spectroscopy

Information about chemical state was determined by X-ray photoelectron spectroscopy. XPS spectra were obtained by a PHI5700/660 Physical Electronics Photoelectron Spectrometer with monochromatic Al Kα X-ray radiation (1486.6 eV). The energy of the electrons was measured with a hemispherical analyzer and resolution of about 0.3 eV. Photoelectron emission was measured from a surface area with a diameter of 800 μm and at a take-off angle of 45°. Due to the occurrence of a charge effect, a neutralizer was used for nonconductive samples. To determine the binding energy, C1s component set at 285 eV was used. Quantification of XPS spectra utilizing peak area and peak height sensitivity factor used to the MultiPak Physical Electronics application. Peak shapes were fitted with the Simpeak software. Outline of the curve fitting is as follows. Select the binding energy range for background subtraction (1). Select the linear method for the background subtraction (2). Select Doniacha-Sunjića peak shape (Doniach and Sunjic 1970) as the peak shape (3) and full width at half maximum for the specific peaks (4). Select the best fitted curve for experimentally obtained core level spectra, which gives the minimum chi square (7). These steps were repeated until the best chi squared was given. The binding energy values (BE) of each component are presented on the spectrum with the estimated error ± 0.3 eV.

Raman spectroscopy

Raman spectra of the studied samples were obtained with a WITec confocal Raman microscope CRM alpha 300R equipped with an air-cooled solid-state laser (λ = 532 nm) and a CCD camera. The excitation laser radiation was coupled to the microscope through a single-mode optical fiber with a 50 mm diameter. An air Olympus MPLAN (100x/0.90NA) lens was used. Raman scattered light was focused onto a multi-mode fiber (100 mm diameter) and a monochromator with a 600 line/mm grating. The spectrometer monochromator was calibrated using the Raman scattering line of a silicon plate (520.7 cm^{-1}). Post-processing analysis including baseline and fluorescence correction as well as cosmic ray removal was done using WitecProjectFour while peak fitting analysis used the GRAMS software package. Peak fitting was done by means of Voigt function with a minimum number of components.

RESULTS AND DISCUSSION

Microprobe analyses

Electron-microprobe analyses were conducted at various locations within the celadonites vein section (Table 1). Calculated formulas are $K_{0.629}Ca_{0.041}(Mg_{0.545}Fe^{2+}_{0.180}Mn_{0.002})(Fe^{3+}_{0.430}Al_{0.95})(Si_{3.755}Al_{0.245})O_{10}(OH)_2$ for emerald-green "celadonite" and $K_{0.766}Ca_{0.031}(Mg_{0.584}Fe^{2+}_{0.134}Mn_{0.001})(Fe^{3+}_{0.562}Al_{0.655})(Si_{3.962}Al_{0.038})O_{10}(OH)_2$ for dark-green "celadonite". Celadonite is defined as a dioctahedral mica of ideal composition $KMgFe^{3+}Si_4O_{10}(OH)_2$ with possible content of a tetrahedral Al (or Fe^{3+}) in the range of 0.0 to about 0.2 atoms per formula unit (Bailey (1980)). However, substantial octahedral variations from this formula can be described by adjectival modifiers, such as aluminian celadonite or ferroan celadonite. According to criteria for the classification of clay minerals (Rieder *et al.* 1998; Drits *et al.* (1997); Tischendorf *et al.* 2007), the samples cannot be considered celadonite, but aluminoceladonite, where an $^{VI}Al(^{VI}Al + {}^{VI}Fe^{3+})$ value is in 0.5–1 range. Here, they are named as aluminoceladonites AlCel 1 and AlCel 2, respectively.

X-ray diffraction

By means of the Rietveld analysis, the semi-quantitative weight fractions of the main minerals in the sample were determined. The emerald-green sample (AlCel 1) contains 73% celadonite, 13% quartz and 14% smectite, the dark green sample (AlCel 2) contains 93% celadonite, 6% quartz and 1% smectite. For the studied aluminoceladonite samples the determination of the unit-cell parameters from the experimental powder XRD patterns was carried out with the aid of experimental d(hkl) values (Text-fig. 1). The calculated unit parameters are presented in Table 2. The dioctahedral nature of the investigated aluminoceladonite was indicated by its d(060) value of 1.509 Å (Text-fig. 1). The relative displacement of the adjacent layers along the *a* axis is characterized by dependence of the I*c*·cos*b*/*a*I value and are the same for both aluminoceladonites, namely 0.367. The deviation of the observed I*c*·cos*b*/*a*I from the ideal 0.333 value (Drits *et al.* 2006) depends significantly on the difference in the size of the vacant and occupied octahedral sites of the 2:1 layer and is related to a high content of Mg and Fe^{3+} (Muller *et al.* 2000). Calculated values of layer-to-layer distances (*c*sin*b*) 9.942 Å (AlCel 1) and 9.935 Å (AlCel 2) as well as lateral dimensions (Table 2) for investigated aluminoceladonite samples are typical for these group of minerals (Muller *et al.* 1999, 2000;

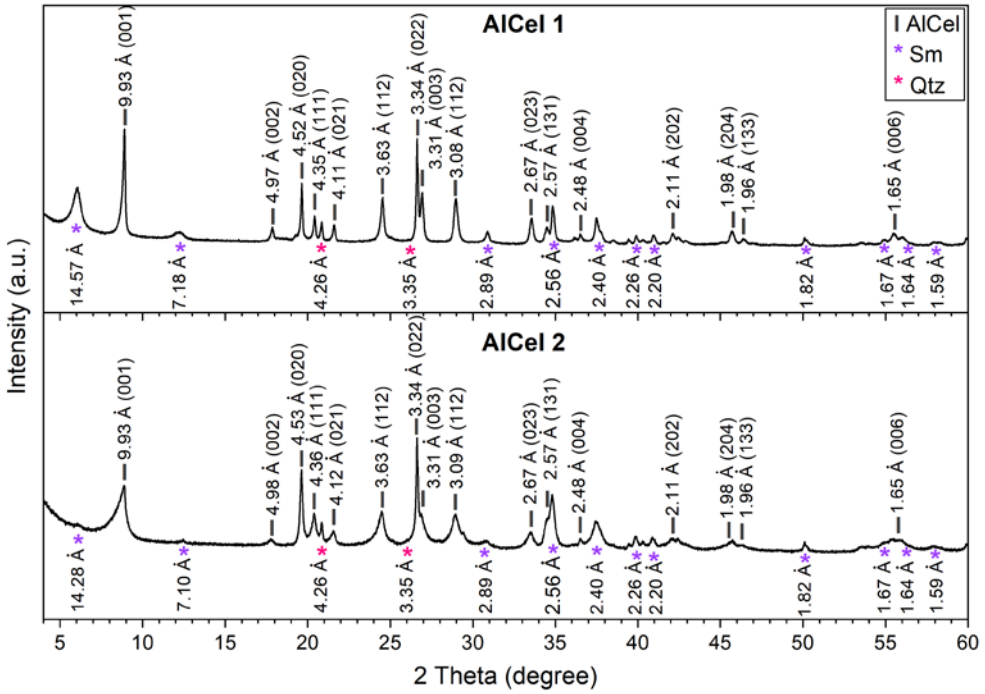

Text-fig. 1. XRD patterns obtained for the investigated aluminoceladonite AlCel 1 and AlCel 2. The hkl indices and calculated d-values are given for each diffraction peak for the alumonoceladonite (AlCel) and d-values are also shown for smectite (Sm) and quartz (Qtz).

Drits *et al*. 2010) but *c*sin*b* values are considerably higher than the values presented for aluminoceladonite in the literature data (Zviagina *et al.* 2015). The reason for that is the following values of csin*b* are basically determined by the mean interlayer distance, which depends on the amount of Al for Si substitution (Drits *et al*. 2010). Accordingly, aluminoceladonites with little or no tetrahedral Al have shorter interlayer distances and as a result, reduced csinb values. It is also worth noting that the d(00l) peak of AlCel 2 is much wider than those of AlCel1. We can suggest that the AlCel 2 sample is in fact aluminoceladonite-rich interstratified aluminoceladonite-smectite (Środoń 1999).

Sample	AlCel 1	AlCel 2
a [Å]	5.2314(6)	5.2314(4)
b [Å]	9.0337(9)	9.0255(7)
c [Å]	10.1260(10)	10.1187(5)
α [°]	90	90
β [°]	100.930(7)	100.934(5)
γ [°]	90	90
V [Å^3]	469.863(1)	469.091(1)
R_p (%)	5.23	4.58
R_{wp} (%)	7.44	6.47
λ^2	9.08	7.62

Table 2. The unit cell parameters and goodness of fit parameters obtained for the studied samples.

^{57}Fe Mössbauer spectroscopy

Obtained Mössbauer spectra for both investigated aluminoceladonite samples consist of broad paramagnetic lines which are hard to separate owing to the overlapping of the spectrum peaks. From this reason these spectra first were fitted using quadrupole splitting (QS) distribution. Such a procedure is especially important when there is a large number of configurations reflecting different neighborhoods or local environment of iron atoms and it can help find the most probable configurations at which the iron can exist in the investigated samples. Spectra of AlCel 1 and AlCel 2 were fitted by two independent density probability distribution of QS. First of them, with the lower values of isomer shift (IS) of approximately 0.30 mm s^{-1} for AlCel 1 and 0.31 mm s^{-1} AlCel 2, corresponds to Fe^{3+} ions in octahedral coordination. The QS peaks and subpeaks can be assigned to different microenvironments as follows: Fe^{3+} *cis* position having quadrupole splitting values lower than 0.80 mm s^{-1} and Fe^{3+} in highly distorted *trans* positions with quadrupole splitting values in range from about 0.80 mm s^{-1} to 1.40 mm s^{-1}. As can be seen on Text-fig. 2, for the AlCel 1 this configuration exists with similar probability whereas for AlCel 2 Fe^{3+} *cis* position prevails. The second part of distribution with

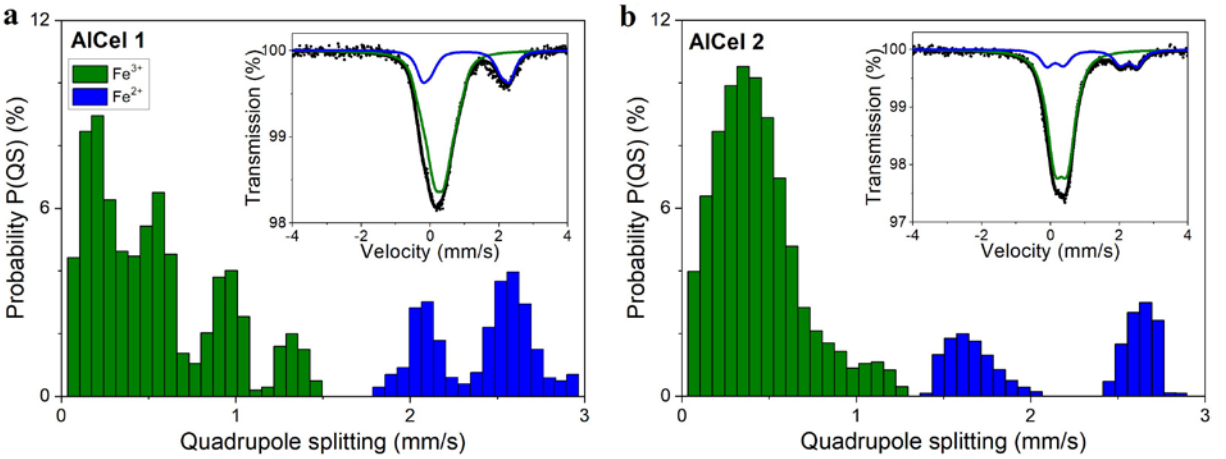

Text-fig. 2. Quadrupole splitting distribution (QSD) obtained for the investigated aluminoceladonite AlCel 1 (a) and AlCel 2 (b) and corresponding their Mössbauer spectra (inserts).

the higher value of IS of 1.04 mm s^{-1} for AlCel 1 and 1.19 mm s^{-1} for AlCel 2 corresponds to Fe^{2+} ions in octahedral coordination and indicated two distinct maxima for both samples. These maxima are located at ~2.10 mm s^{-1} and ~2.60 mm s^{-1} for AlCel 1. For AlCel 2, peaks are located at 1.65 mm s^{-1} and 2.65 mm s^{-1}. Ferrous Fe doublets cannot be assigned to *cis* and *trans* sites. Rancourt (1994) goes on to demonstrate that Mössbauer spectra of 2:1 layer silicates cannot resolve the octahedral Fe^{2+} *cis* (M2) and *trans* (M1) sites. It is important to note that he was not the first to reach this conclusion. Studies by Goodman (1976), Mineeva (1978), Ballet and Amthauer (1986) and others had earlier come to similar conclusions using the electric field gradient (EFG) calculations for micas. This conclusion was also confirmed in recent works (Redhammer *et al.* 2000; Dyar 2002). The ferrous quadrupole splitting distribution components do not correspond to a specific crystallographic site (M1 or M2), but arise from local geometric and/or electronic distortion environments around the Fe atoms within the octahedral sheet of the micas. Based on QSDs analysis, the Fe^{3+}/Fe_{tot} ratio is 0.739 for AlCel 1 and 0.797 for AlCel 2 sample.

Taking into account the calculated QS histograms (Text-fig. 2) which clearly are multimodal it is tempting to associate the distinct maxima to the different iron sites. For that purpose an attempt was made to fit the obtained spectra by a superposition of six doublets, whose parameters are listed in Table 3. Both the measured Mössbauer spectra and the fitted components for the investigated samples are presented in Text-fig. 3. For AlCel 1 the Fe^{3+}/Fe_{tot} ratio is 0.705, whereas for AlCel 2 it is 0.803. These ratios are almost the same as those from QSD calculations. The obtained values of isomer shifts for ferric components (Table 3) indicate that neither of the studied samples contained Fe^{3+} in the tetrahedral sheet because the upper limit of isomer shift value for Fe^{3+} in tetrahedral coordination is approximately 0.25 mm s^{-1}, whereas the lower limit for octahedral Fe^{3+} is approximately 0.29 mm s^{-1} (Dyar *et al.* 2006). Additionally, based on the obtained hyperfine parameters (Table 3), we can also exclude the presence on the Mössbauer spectra of components connected with Fe in quartz structure (Czaja et al. 2017). To sum up, hyperfine parameters of fitted components obtained from discrete analysis of Mössbauer spectra lead us to relate them directly with iron sites in the structure of the investigated aluminoceladonite.

Due to the above, AlCel 2 contains about 19% Fe^{2+} in octahedral sites. The majority of the iron is Fe^{3+} in the *cis*-OH (M2*)* site (Drits *et al.* 1996; Dainyak *et al.* 2006) with QS ~ 0.19 and 0.49 mm s^{-1}. Doublet with large QS ~ 0.81 mm s^{-1} can be ascribed to Fe^{3+} ions in *trans*-OH (M1) sites. The value of 1.29 mm s^{-1} is a rather large quadrupole splitting to be the *trans*-OH (M1) sites, and was ascribed to dehydroxylated sites (Dainyak and Drits 1987). AlCel 1 contains a little more (~30%) Fe^{2+} in comparison to the previous one, but also almost equally divided between the two sites with different local geometric distortion around these ions. The majority of all Fe^{3+} occupies *cis*-OH (M2) site with QS ~0.17 and 0.54 mm s^{-1}. The rest of the Fe^{3+} ions is located in the *trans*-OH (M1) sites which are characterized by large values of QS, which are 1.01 and 1.44 mm s^{-1} (Bowen *at al.* 1989; Redhammer *et al.* 2005).

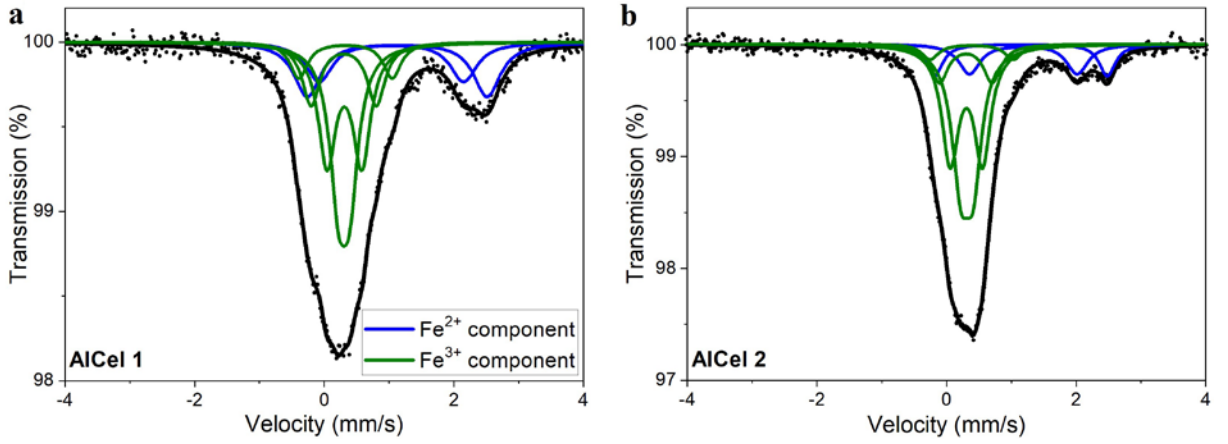

Text-fig. 3. Mössbauer spectra obtained for the investigated aluminoceladonite AlCel 1 (a) and AlCel 2 (b). The fitted subspectra (colored lines) are presented on the investigated spectra together with the overall fit (black line).

On the basis of the result of the crystal-chemical models (Tsipursky and Drits 1984; Dainyak *et al.* 2004, 2006; Zviagina *et al.* 2015), where authors used an empirical relationship between the quadrupole splitting values and the nature of the nearest cation neighbours, the values of the fitted quadrupole doublets Fe^{3+} and Fe^{2+} may correspond to specific local cationic arrangements around Fe^{3+} and Fe^{2+} ions., i.e. the inner doublets with quadrupole splitting of 0.17 and 0.19 mm s^{-1} assigned to Fe^{3+} with three nearest Fe^{3+} ions. The quadrupole splitting of 0.49 and 0.54 mm s^{-1} reflects Fe^{3+} in the arrangement of $MgFe^{2+}Fe^{3+}$ and $2AlFe^{3+}$, respectively. The value of QS, which is 0.81 mm s^{-1}, is close to the theoretical value responsible for Fe^{3+} in the 3Al arrangement. The large values of quadrupole splitting, i.e. 1.01, 1.29 and 1.44 mm s^{-1}, which are associated with the *trans*-OH (M1) sites, are the consequence of Fe^{3+} in arrangements $AlMgFe^{3+}$, $2Fe^{3+}Mg$ and 2AlMg, respectively. For AlCel 1, a higher proportion of components related to the Al environment than to the AlCel 2 is observed due to higher Al content. It also confirms the correctness of the applied theoretical model. A similar interpretation of the quadrupole splitting can be made for the local cation arrangements around Fe^{2+} ions. The smallest value of QS (1.66 mm s^{-1}) is connected with the arrangement of $2MgFe^{2+}$ ions and the highest value (2.77 mm s^{-1}) with $2Fe^{3+}Fe^{2+}$. Intermediate QS reflect an almost similar arrangement, i.e. 2.23 mm s^{-1}, which is the result of $2Fe^{2+}Al$, and 2.66 mm s^{-1} is the result of $AlMgFe^{2+}$ local cation distribution. The above interpretation of Mössbauer spectra suggests that Fe^{3+} ions are not randomly located in the structure of the studied samples but in some position within the preferred neighbourhood. As can be seen on Mössbauer

Mineral	Component	IS (mm s^{-1})	QS (mm s^{-1})	G (mm s^{-1})	A (%)	Arrangement
AlCel 1	1 (Fe^{3+})	0.31	0.17	0.33	26.3	$3Fe^{3+}$
	2 (Fe^{3+})	0.31	0.54	0.33	24.3	$2AlFe^{3+}$
	3 (Fe^{3+})	0.30	1.01	0.33	12.8	$AlMgFe^{3+}$
	4 (Fe^{3+})	0.33	1.44	0.33	7.4	2AlMg
	5 (Fe^{2+})	1.04	2.23	0.50	12.6	$2Fe^{2+}Al$
	6 (Fe^{2+})	1.13	2.77	0.50	16.9	$2Fe^{3+}Fe^{2+}$
AlCel 2	1 (Fe^{3+})	0.31	0.19	0.32	33.8	$3Fe^{3+}$
	2 (Fe^{3+})	0.31	0.49	0.32	31.7	$MgFe^{2+}Fe^{3+}$
	3 (Fe^{3+})	0.30	0.81	0.32	10.8	3Al
	4 (Fe^{3+})	0.39	1.28	0.32	4.4	$2Fe^{3+}Mg$
	5 (Fe^{2+})	1.19	1.66	0.40	10.6	$2MgFe^{2+}$
	6 (Fe^{2+})	1.15	2.66	0.32	8.7	$AlMgFe^{2+}$

Table 3. The Mössbauer hyperfine parameters of the investigated aluminoceladonite samples. Absolute errors are estimated at ±0.5% for doublet areas (A), ±0.01 mm s^{-1} for isomer shift (IS) and for full line width at half maximum (G), ±0.02 mm s^{-1} for quadrupole splitting (QS).

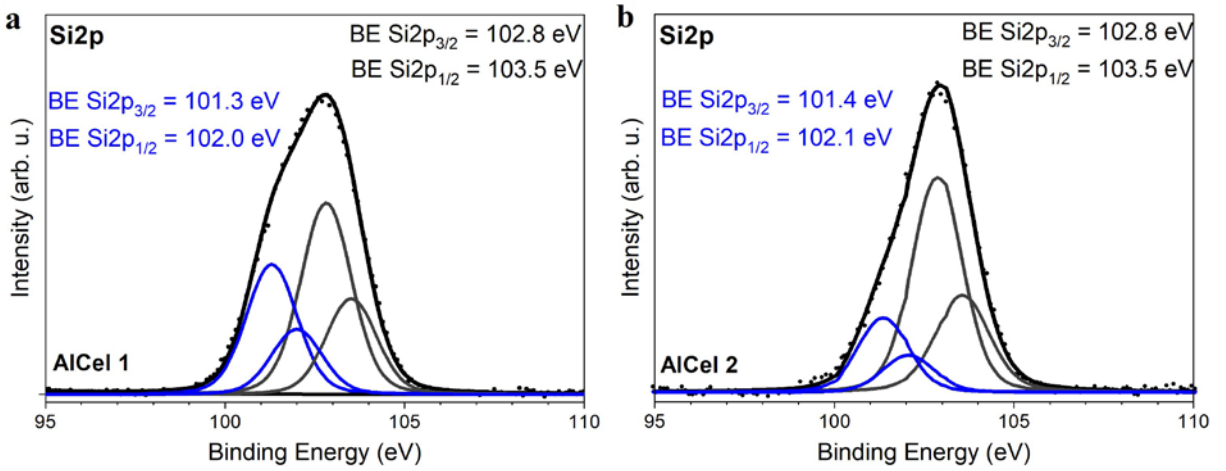

Text-fig. 4. XPS spectra showing the Si2p region with relative peak deconvolutions (colored lines) obtained for AlCel 1 (a) and AlCel 2 (b).

spectra and in Table 3, the lines of Fe^{2+} doublets are much broader than those of Fe^{3+}. This indicates some disorder in Fe^{2+} ion environment and its different local surrounding.

X-ray photoelectron spectroscopy

The interpretation of the XPS spectra of the investigated aluminoceladonite can provide information on the molecular environment, i.e., oxidation state, multiplet structure, chemical bonding, etc. with an error of <10%. This can enable visualization of cation arrangement in a layer-silicate structure. XPS spectra obtained in the region of the Si2p, Al2p, Fe2p, K2p and O1s core levels are displayed as a plot of electron binding energy vs. intensity are shown in Text-figs 4–8.

In many silicates, Al^{3+} and/or Fe^{3+} substitution for Si in the tetrahedral site has been found (Seyama and Soma 1985); Vantelon *et al.* 2009). The Si2p binding energies (referenced to Cls) lie in the range of 100.9–103.35 eV (Elmi *et al.* 2014, 2016), but the component assigned to Si^{4+} in tetrahedral coordination is localized from 102.36 to 102.16 eV. The Si2p spectrum should show a doublet branching ratio of 2:1 for Si $2p_{3/2}$ to Si $2p_{1/2}$ with a spin-orbit splitting of about 1 eV difference. Values of Si2p binding energies show Si^{4+} in tetrahedral coordination (Bhattacharyya 1993; Biino and Gröning 1998; Elmi *et al.* 2014, 2016). These spectra in Text-fig. 4 present two Si2p (3/2, 1/2) doublets. The silicon binding energy shows that different populations of Si atoms correlate with substitutions in the tetrahedral sheet. A lower Si2p binding energy may result from a negative charge increase on the silicate framework as a result of Si^{4+} replacement by Al^{3+}. The Si2p binding energy of layer silicates, in which some Si is substituted by Al, is 0.7 eV lower than that of the compounds containing only Si in the tetrahedral site (Elmi *et al.* 2016). The primary reason for the Si2p binding energy decrease is the apparent reduction in the silica network polymerization driven by the Si content. The obtained results indicate that the tetrahedral sheet contains only Si in tetrahedral with some Al^{3+} substitution. On the basis of the area ratio of Si2p components we can calculate the ratio of Si^{4+} in tetrahedral coordination to Al^{3+}. For AlCel 1, this ratio is 60/40, whereas for AlCel 2 it is 72/28.

The Al2p lines are located at the binding energies in-between 70 eV to 77 eV for both of the aluminoceladonite samples (Text-fig. 5). Because these spectra have evident asymmetry in the peak shape, they were decomposed into two Al2p doublets. In layer silicates, Al atoms can occur in both tetrahedral and octahedral sites so each of these doublets will reflect different Al coordination. The obtained Al binding energy value is very close to both fourfold and sixfold coordination. However, an octahedral sheet must compensate for the charge of two relatively negative and adjacent tetrahedral sheets. The positive nature of the octahedral sheet coupled with the relatively negative silicate sheet results in more ionic Al-O bonds. The enhanced ionicity of the Al-O bond may be reflected in the relatively higher Al2p binding energy value. Also, the presence of OH and/or F enhances the positive character of the Al resulting in a moderate increase in the Al2p binding energy (Barr *et al.* 1997). That is why the $Al2p_{3/2}$ line located at

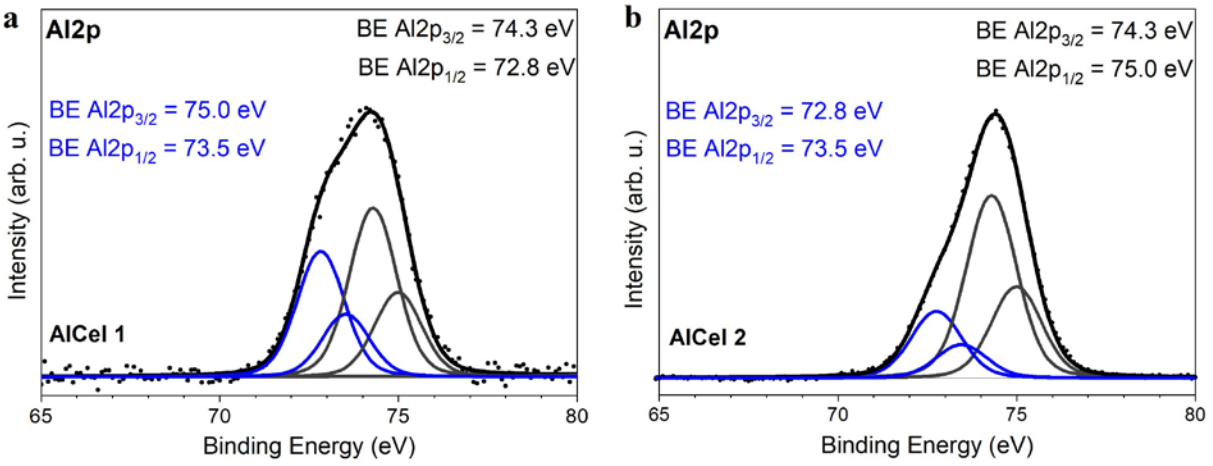

Text-fig. 5. XPS spectra showing the Al2p region with relative peak deconvolutions (colored lines) obtained for AlCel 1 (a) and AlCel 2 (b).

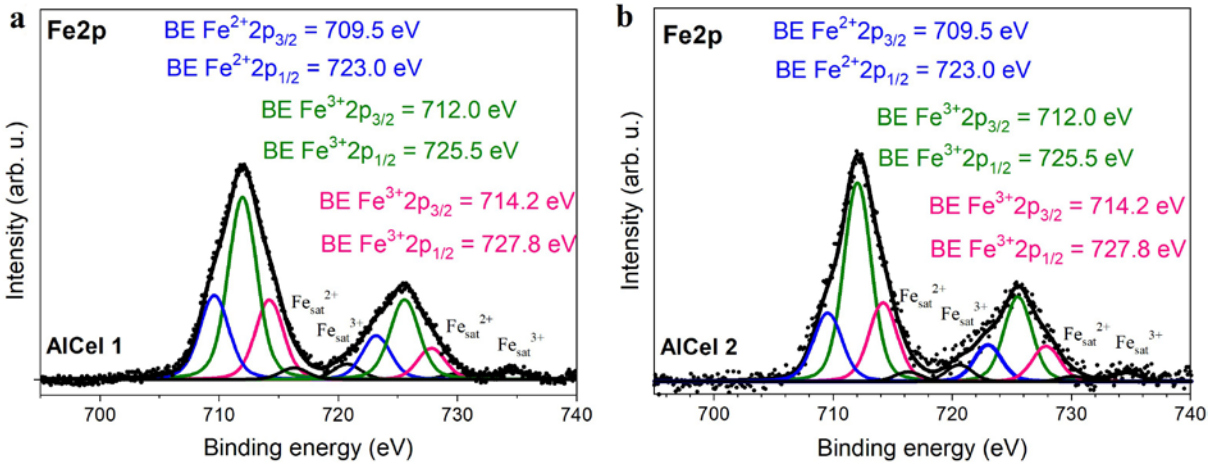

Text-fig. 6. XPS spectra showing the Fe2p region with relative peak deconvolutions (colored lines) obtained for AlCel 1 (a) and AlCel 2 (b).

binding energy of 74.3 eV relates to Al present in octahedral coordination, while the other one with BE of 72.8 eV arises from Al in tetrahedral coordination. The ratios of Al ions in tetrahedral sites to these in octahedral are 43/57 and 27/73 based from area ratios of Al2p components, for AlCel 1 and AlCel 2, respectively. These values are very close to those obtained for Si2p, which is compatible with our interpretation. A small difference can also arise from the presence of a low amount of quartz in the investigated samples. The above results indicate that the tetrahedral sheet contains not only Si^{4+} but also Al^{3+} ions which confirms chemical and XRD analyses.

The Fe2p spectra are characterized by doublet structures relating to spin-orbit splitting between $2p_{1/2}$ and $2p_{3/2}$ states. In addition to the multiplet structures, the shake-up satellite peaks are present, arising from intrinsic energy losses when the photoelectron leaves the hosting atom. Deconvolution in both samples of the Fe2p peak (Text-fig. 6) shows three main components. The first, a weaker one, related to the Fe^{2+} valence state is a doublet with binding energies $Fe2p_{3/2}$ = 709.5 eV and $Fe2p_{1/2}$ = 723 eV. The second, the highest one, is characteristic of the Fe^{3+} state observed as a multiplet with binding energies of the main component equal to $Fe2p_{3/2}$ = 712.0 eV and $Fe2p_{1/2}$ = 725.5 eV. The third component at BE of 714.4 eV is associated with Fe^{3+} state. Area ratios of peaks at BE of 712.0 eV and 714.2 eV are 53/23 for AlCel 1 and 62/20 for AlCel 2. The obtained proportion is almost the same as those obtained from Mössbauer analysis (Table 3) and reflects the M2/M1 ratio of Fe^{3+} ions in octahedral positions. About 2 eV distance between these components can be a result of dehydroxylated

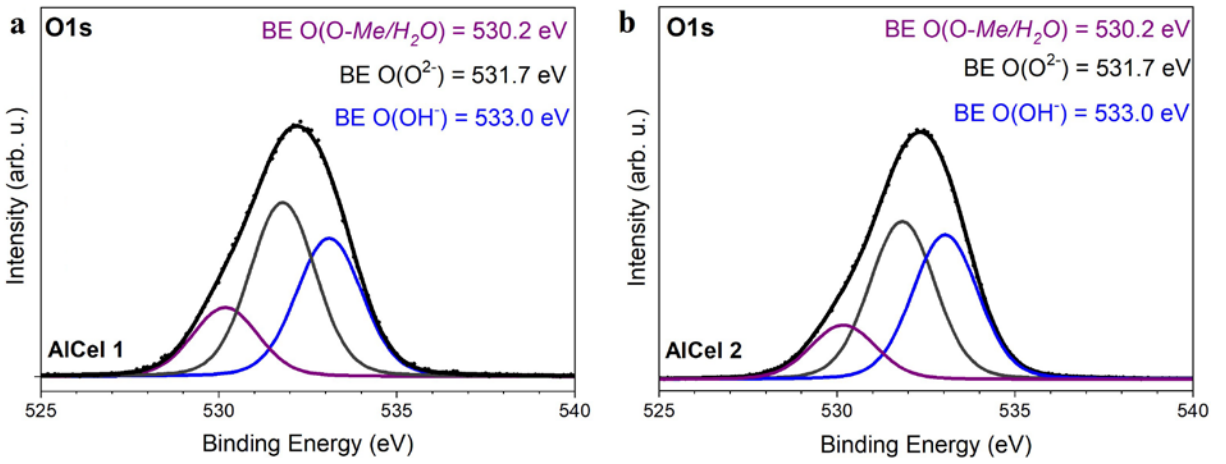

Text-fig. 7. XPS spectra showing the O1s region with relative peak deconvolutions (colored lines) obtained for AlCel 1 (a) and AlCel 2 (b).

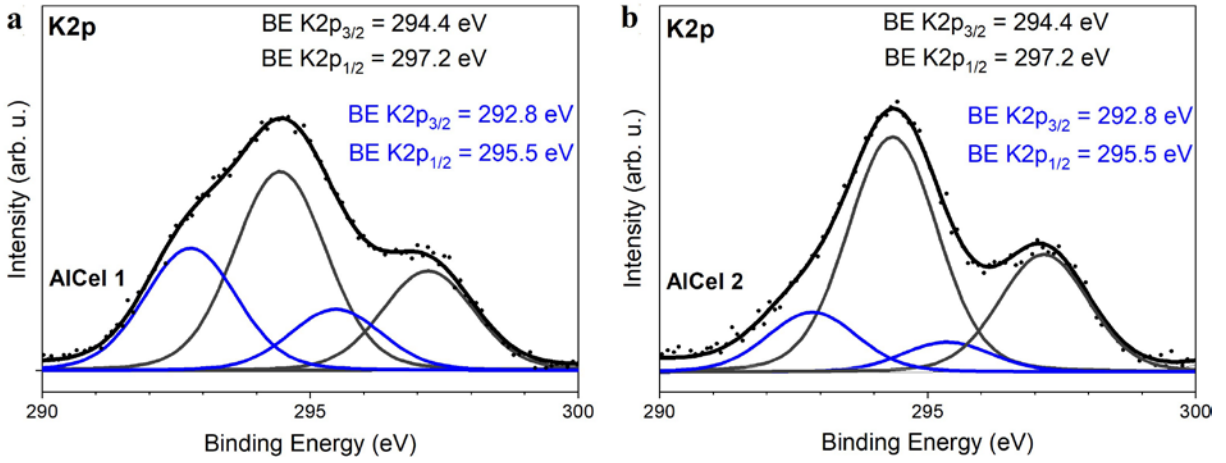

Text-fig. 8. XPS spectra showing the K2p region with relative peak deconvolutions (colored lines) obtained for AlCel 1 (a) and AlCel 2 (b).

sites. Fe^{2+}/Fe^{3+} ratios based on the area ratio of Fe2p, were determined to be 0.30 for AlCel 1 and 0.22 for AlCel 2.

Text-figure 7 displays XPS spectra of O1s regions of the investigated aluminoceladonite samples. The O1s core-level XPS line comprises three separate peaks located at binding energies of 530.2, 531.7 and 533.0 eV, which can be related to the existence of different forms of oxygen bondings. The most intense line at a binding energy of 531.7 eV is typical of the of lattice oxygen O^{2-} (Kloprogge and Wood 2018). The peak positioned at the highest binding energy of 533 eV corresponds to hydroxyl oxygen OH^- (Schingaro *et al.* 2013). The lowest intensity line at 530.2 eV is due to the presence of O-Me bonds or small amount of interlayer H_2O (Tissot and Li 2016).

Potassium K2p has clearly spaced spin-orbit components (Text-fig. 8). Because the obtained K2p spectra have asymmetric peak shapes, they were decomposed into two K2p doublets. The $K2p_{3/2}$ binding energies are at 294.4 eV and 292.8 eV for both of the aluminoceladonite samples and are connected with the K^+ ions, which occupy interlayer sites between two 2:1 layer. The origin of the "extra" K2p doublet is not well understood. On the basis of the chemical analysis, we might conclude that it results from the presence of calcium substitution or interlayer H_2O, which modifies the chemical environment in the interlayer configuration of the analyzed micas (Table 1). The area ratios for the obtained doublets of K2p are 62/38 for AlCel 1 and 80/20 for AlCel 2, which results from the ratio of K^+ and Ca^{2+} ions, respectively. The doublet with smaller contribution probably arises from K^+ ions being replaced by Ca^{2+} ions in interlayer sites. On the other hand, the calcium content is too high compared to the results of

the chemical analysis. It may suggest that not only Ca^{2+} is substituting the K^{+} in interlayer sites but that in these sites also, a small amount of structural water is present.

Raman spectroscopy

The chemical composition and crystal-chemical recalculations of analyzed samples suggested minerals affiliation to the 2:l clay minerals family with tetrahedral–octahedral–tetrahedral (T-O-T) layer arrangement bonded together by large interlayer cations A (A = Na^{+}, K^{+}) (Richardson and Richardson 1982; Redhammer *et al*. 2000; Brigatti *et al.* 2013). Within this type of structure, the individual tetrahedra are linked through the bridging (= basal) oxygen, while the octahedral cations are coordinated by four non-bridging (= apical) oxygen originated from upper and lower tetrahedral sheets as well as hydroxyl ions located close to the center of six-fold rings (Li *et al.* 2011). Tetrahedral positions, as confirmed previous chemical methods, are occupied by *M*Tet = Si^{4+} and Al^{3+}, while the octahedral ones by trivalent cations *M*Oct = Al^{3+}, Fe^{3+}, (+vacant) occurring in dioctahedral configuration or divalent cations *M*Oct = Fe^{2+}, Mg^{2+} (Madejová *et al.* 2017). This information is extremely crucial in the context of the Raman data interpretation. Here, the correlation between crystal structure and optical spectroscopy (Infrared, or Raman) can be realized in the form of the individual band analysis represented by the vibration of atoms occupying the tetrahedral and/or octahedral positions. According to this assumption and literature data, the minerals of the 2:1 family in the high-frequency region are characterized by the stretching and bending vibrations of hydroxyl groups coordinating the octahedra, which are located in the 3700–3500 cm^{-1} region. These bands are only weakly coupled with other vibrations appearing within such kind of clay mineral structure (Farmer 1974; Gates 2005; Petit 2005). This type of structure seems to be also featured by fixed interlayer spacing, which potentially makes impossible molecular water incorporation. However, according to XPS analysis, a small content of water incorporated into the crystal structure can not be excluded (see appropriate paragraph). Apart from the problem of water, the fitting analysis carried out for both spectra in the hydroxyl-stretching range revealed five bands slightly shifted relate to each other with maxima at 3627, 3608, 3582, 3564, 3541 cm^{-1} (AlCel 1) and 3620, 3609, 3588, 3567, 3542 cm^{-1} (AlCel 2) (Text-fig. 9). Unfortunately, their interpretation as being due to various possibilities of cationic substitution ought to be treated with a high dose of uncertainty even though the data correlate with theoretical considerations (Velde 1983); Robert and Kodama 1988; Martínez-Alonso *et al.* 2002b). The uncertainty results from the nature (= the formal charge and electronegativity) of octahedral cations bonded to the OH and neighboring tetrahedral apical O atoms, which may act a role of acceptors for hydrogen bonds (Li *et al.* 2011). Despite this and considering the previous analysis performed for clay minerals (Zviagina *et al.* 2004, 2015), we propose assignment of hydroxyl groups located at their neighboring SiO_4 tetrahedron to the highest-frequency band, while the others are assigned to the (Mg_2, Fe^{2+})-OH or (Mg, Fe_2^{2+})OH, (Al^{3+}, Fe)$^{3+}$OH, (Fe_2^{3+})OH and (Mg, Fe^{3+})-OH) groups, respectively. In this place it is worth noting that these assignments draw attention to the problem of stoichiometry and charge-balance of the structure, with local structure modifications enforced by different cations and the impact of chemical environment on the molecular ordering within individual clay sheets. In this context, a slight difference in the band intensity and full width at half maximum observed between AlCel 1 and AlCel 2 might result from a variability in the OH group environment, variability of octahedral cationic substituents, incomplete protonation during the crystallization corresponding to structural defects linked to the disturbance of the ideal T-O-T configuration or it might even be a polarization effect. It is, however, worth noting that Raman data ought to be correlated with the chemically-sensitive microprobe and XPS techniques (see appropriate paragraphs in the text) to confirm or exclude a possible deprotonation effect or to estimate the impact of the concentration of the hydroxyl groups. Another explanation lies in the chemical correlation with the aforementioned hypothetical vibrations of individual groups. In this context, the strongest bands found at 3609 and 3567 cm^{-1} might indicate an excess of Fe^{3+} in some of the octahedral sites as well as the simultaneous occupation of the octahedral sites by Mg^{2+} and Fe^{2+}. This hypothesis seems in accord with the chemical data indicating the elevated concentration of iron in AlCel 2 due to higher content in relation to Al and Mg. Moreover, the spectrum of AlCel 2 with two dominant bands corresponds to a better ordering of cations in the octahedral sheet. The Raman fingerprint region consists of many overlapping bands with a variable intensity (Text-fig. 9). An interesting fact worth mentioning here is that the weak coupling modes referring to tetrahedrally coordinated cations, especially *M*Tet = Si^{4+}, activate symmetric

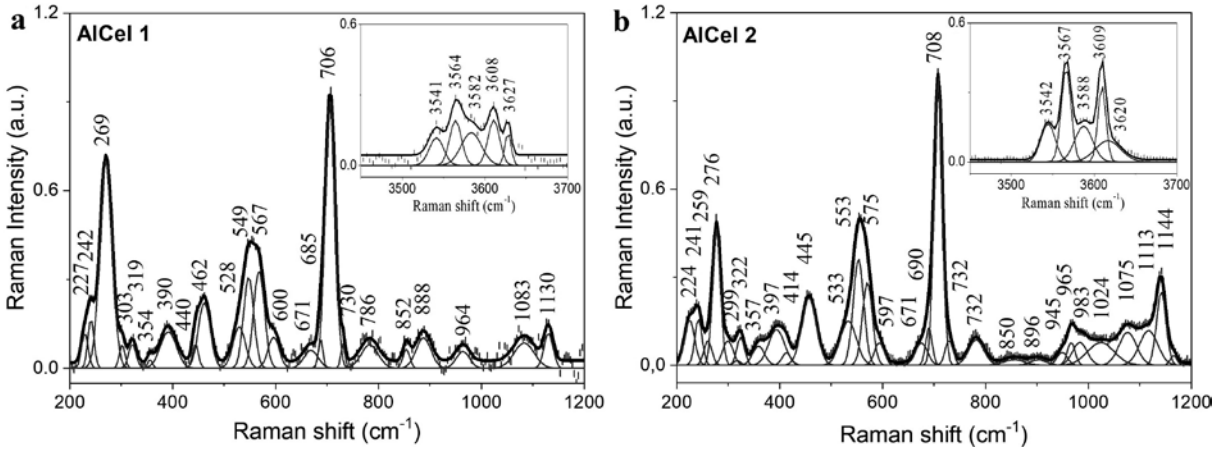

Text-fig. 9. Raman spectra of the investigated aluminoceladonite samples AlCel 1 a) and AlCel 2 b) after cosmic ray removal, fluorescence and baseline correction, as well as peak fitting analysis. The calculated values of band frequency with the estimated error of ± 3 cm^{-1} are visible on the spectra.

and asymmetric internal stretching vibration of the ν(Si-O) and T-O-T bending modes, especially in the 1200–700 cm^{-1} region. In turn, deformational modes of tetrahedrally cations δ(O-Si-O) that correspond to the bands located in-between 600–400 cm^{-1} are usually strongly coupled with vibrations of the octahedral atoms and/or hydroxyl groups (Farmer 1974). As a result of the chemical analysis of studied samples in relation to other clay minerals, it is crucial to consider the presence of magnesium, aluminum, and iron as well as their impact on the local arrangement within the sheets. As a result, according to the literature reports, we can expect the appearance of the bands related to the δ(Si-O) modes within tetrahedra (~480 cm^{-1}) that partially overlap with δ(Si-O-M_{Oct}) once. In turn, magnesium (Mg^{2+}) in the octahedral position may imply the shift of the band position towards higher frequencies (540–510 cm^{-1}), especially in relation to the aluminum (Al^{3+}) and iron (Fe^{3+}) that occupy the octahedral position (Michalski *et al.* 2010). Another kind of vibration results from the coordinated bending modes along the Si-O-M_{Oct}, which should imply the appearance of weak bands in-between 450–400 cm^{-1} (M_{Oct} = Mg^{2+}) and 670–550 cm^{-1} (M_{Oct} = Al^{3+}, Fe^{3+}) (Bishop *et al.* 2017). Low-frequency bands observed usually below 400 cm^{-1} correspond to the lattice vibration of the main backbone fragments as well as hydroxyl modes.

As a result of the literature and above-mentioned data, the main bands found in the case of both aluminoceladonites in the 1110–950 cm^{-1} region correspond to the asymmetric stretching vibrations within the tetrahedral sheet. According to the fitting analysis, we propose assignment of the bands centered at 1130 cm^{-1} (AlCel 1) and 1144, 1113 cm^{-1} (AlCel 2) to the Si-O modes perpendicular to the SiO_4 tetrahedral sheet, whereas 1083, 964 cm^{-1} (AlCel 1) and 1075, 1024, 983, 965 cm^{-1} (AlCel 2) are assigned to in-plane Si-O stretching modes. According to microprobe chemical analysis, the presence of aluminum in the tetrahedral position may imply deformation of the tetrahedral and lead to band shift toward higher and lower frequencies. In addition, it may slightly modify their number and intensity, comparing our data with the literature (Li *et al.* 2011). This behavior is seen when comparing two samples through the band splitting found in the vicinity of the most intense band centered at 706 cm^{-1} (AlCel 1 with Al↑ in T-position) and 708 cm^{-1} (AlCel 2 with Al↓ in T-position) ascribed to the symmetric stretching vibration within silica tetrahedra (Text-fig. 9). Hydroxyl bending modes may correspond to the low intense bands of the 900–750 cm^{-1} region. According to the previously suggested interpretation of the hydroxyl region, we suggest the assignment of deformational modes involving octahedral cations as (Al, Fe^{3+})-OH, ($Fe^{3+}{}_2$ OH, (Mg, Fe^{3+})-OH to the bands at 888, 852, 786 cm^{-1} (AlCel 1) and 896, 850, 783 cm^{-1} (AlCel 2). It is interesting that their positions are slightly shifted (~5 cm^{-1}) according to the literature, probably due to uncharged-balanced structure and diverse cationic substitutions (McKeown *et al.* 1999; Madejová *et al.* 2017). Three low intense bands found after fitting analysis at 730, 685, 671 cm^{-1} (AlCel 1) and 732, 690, 671 cm^{-1} (AlCel 2) originate from disturbance of the ideal tetrahedral configuration as a result of signal overlapping of the symmetric stretching ν(Si-O)

with ν(Si-O-Al), δ(Fe-OH) or ν(M_{Oct}-O) vibrations (Kloprogge (2017)). Another explanation of the band arrangement in this spectral fragment seems that it may be correlated with the uncharged-balanced structure due to non-stoichiometry, or disorder of the ideal 2:1 arrangement.

A scheme of band arrangement in the case of both analyzed samples below 600 cm^{-1} is more or less similar in each case, whereas it is difficult to assign a specific type of vibration to the individual bands observed on the Raman spectra (Text-fig. 9). The most visible differences correspond to the full width at half maximum, which are especially well seen in the case of the band in the vicinity of 550 cm^{-1} (Text-fig. 9). What is more, according to the fitting analysis, those bands are splitting into four components with maxima centered at 600, 567, 549, 528 cm^{-1} (AlCel 1) and 597, 575, 553, 533 cm^{-1} (AlCel 2). All of bands, taking into account the literature, may be related to the deformation δ(O-M_{Oct}-O), δ(O-T_{Tet}-O) or δ(Si-O-M_{Oct}) modes, wherein their origin cannot be clearly interpreted due to its overlapping character and the variability of the cation substitutions in the octahedral positions. Thus, another experimental technique is needed to shed more light on such a problem and help in ambiguous band assignments. At this point, it is worth emphasizing that XRD and XPS analysis showed the presence of aluminum in octahedral and tetrahedral positions, while XPS and Mössbauer pay attention to the distribution of Fe^{2+} and Fe^{3+} iron in the aluminoceladonite layers (see the corresponding paragraphs in the text). This information somehow helps to interpret the position of the bands in this region as well as to shed more light on the possible effect of deprotonation or charge balancing within the layers of celadonite. As a result, we assume that the observed broadening in case of AlCel 1 results from an excess of octahedral aluminum and uncharged balanced octahedral sheets. We can also propose band's assignment of the high-frequency bands in-between 600–560 cm^{-1} to the deformational modes δ(O-Al_{Oct}-O), δ(O-Mg-O) that overlap with δ(OAl_{Tet}O) as well as the δ(SiOM_{Oct}), δ(O-Fe-O) or δ(Si-O-Si) to the bands with similar intensity centered between 560–500 cm^{-1}. Finally, analysis of other bands below 500 cm^{-1} seems to be uncertain in interpretation due to the mixed vibrational character involving silicon-oxygen network and octahedral cations (Farmer 1974; Russell and Fraser 1994). Here, Raman spectra in low-frequency range are affected by deformational and translational modes attributed to δ(O-Si-O), δ(Si-O-Si) which positions correspond to the type of octahedral cationic substitutions, stoichiometry, number of vacancies. Those modes may overlap with deformational vibration of δ(O-M_{Oct}-O), asymmetric deformations of the MO_6 groups (Rinaudo *et al.* 2004) or symmetric stretching of O-H-O linkages (Loh 1973).

CONCLUSIONS

Mössbauer, Raman, and X-ray photoelectron spectroscopies, were used for characterization of elements' local environments in dioctahedral 2:1 Fe-bearing aluminoceladonites. These methods present new constraints on the characterization and interpretation obtained from surface and bulk sensitive techniques. The obtained compositions of the investigated aluminoceladonite samples were $K_{0.629}Ca_{0.041}(Mg_{0.545}Fe^{2+}_{0.180}Mn_{0.002})(Fe^{3+}_{0.430}Al_{0.95})(Si_{3.755}Al_{0.245})O_{10}(OH)_2$ for emerald-green and $K_{0.766}Ca_{0.031}(Mg_{0.584}Fe^{2+}_{0.134}Mn_{0.001})(Fe^{3+}_{0.562}Al_{0.655})(Si_{3.962}Al_{0.038})O_{10}(OH)_2$ for dark-green. Chemical analyses and diffraction methods yielded data only on the averaged composition of cations in the unit-cell sites, ignoring possible short-range ordering. XPS data provided information about oxidation state, chemical bonding or ion distributions for the studied phyllosilicates. As a result, tetrahedral or octahedral coordination of Al^{3+} and Si^{4+} was shown. The interpretation of K2p spectra indicates the possibility of other cationic substitution (e.g., Ca^{2+}) in interlayer sites, typically occupied by K^+ in celadonite. Although X-ray photoelectron spectroscopy is a surface sensitive technique, the obtained results agree with chemical analysis. Importantly, this study shows that the results of the chemical analysis can be visualized as cation arrangements by XPS results. These results are confirmed and specified by the Mössbauer and Raman spectroscopy. All used techniques indicate that Fe prefers a definite position and specific local surrounding i.e. *cis*-OH (M2), and Fe^{3+} ions in the arrangement of $3Fe^{3+}$ ions or $MgFe^{2+}Fe^{3+}$ and $2AlFe^{3+}$. The result of these studies create new possibilities to find out more about cation distribution and cationic substitution in a structure of layer silicates.

Acknowledgements

This work had financial support by the NCN (Poland), on the basis of Decision No. DEC-2018/02/X/ST10/00662. The authors want to thank the anonymous reviewers for there valuable comments.

REFERENCES

Bailey. S. 1980. Summary of recommendations of AIPEA nomenclature committee on clay minerals. *American Mineralogist*, **65**, l–7.

Ballet, O. and Amthauer, G. 1986. Room-temperature Mössbauer study of the EFG tensor at the iron sites in sheet silicates. *Journal of Physics C: Solid State Physics*, **19**, 7099–7112.

Barr. T., Seal, S., Wozniak, K. and Klinowaki J. 1997. ESCA studies of the coordination state of aluminum in oxide environments. *Journal of the Chemical Society, Faraday Transactions*, **93**, 181–186.

Besson. G. and Drits, V.A. 1997a. Refined relationship between chemical composition of dioctahedral fine-grained mica minerals and their infrared spectra within the OH stretching region. Part 1. Identification of the OH stretching vibrations. *Clays and Clay Minerals*, **45**, 158–169.

Besson, G. and Drits, V.A. 1997b. Refined relationship between chemical composition of dioctahedral fine-grained mica minerals and their infrared spectra within the OH stretching region. Part 2. Main factors affecting OH vibrations and quantitative analysis. *Clays and Clay Minerals*, **45**, 170–183.

Bhattacharyya, K. 1993. XPS study of mica surfaces. *Journal of Electron Spectroscopy and Related Phenomena*, **63**, 289–306.

Biino, G. and Gröning, P. 1998. Cleavage mechanism and surface chemical characterization of phengitic muscovite and muscovite as constrained by X-ray photoelectron spectroscopy. *Physics and Chemistry of Minerals*, **25**, 168–181.

Bishop, J., Michalski, J. and Carter, J. 2017. Remote Detection of Clay Minerals. In book: *Infrared and Raman spectroscopes of Clay Minerals*, **84**, 82–514.

Brigatti, M., Frigieri. P. and Poppi, L. 1998. Crystal chemistry of Mg-, Fe-bearing muscovites-2M_1. *American Mineralogist*, **83**, 775–785.

Brigatti, M., Galan, E. and Theng, B. 2013. Structure and mineralogy of clay minerals. Chapter 2, In: Bergaya F. and Lagaly G. (Eds.), Handbook of Clay Science, Part A: Fundamentals, second ed, 21–82. Elsevier; The Netherlands.

Bowen, L., DeGrave, E., Reid, D,. Graham, R. and Edinger, S. 1989. Mössbauer sudy of a California Desert celadonite and its pedogeniclly-related smectite. *Physisc and Chemistry of Minerals*, **16**, 697–703.

Czaja, M., Mariola Kądziołka-Gaweł, M., Konefał, A., Sitko, R., Teper, E., Mazurak, Z. and Sachanbiński, M. 2017. The Mössbauer spectra of prasiolite and amethyst crystals from Poland. *Physics and Chemistry of Minerals*, **44 (5)**, 365–375.

Dainyak, L. and Drits, V. 1987 Interpretation of Mössbauer spectra of nontronite, celadonite, and glauconite. *Clays and Clay Minerals*, **35**, 363–372.

Dainyak, L., Drits V. and Lindgreen, H. 2004. Computer simulation of octahedral cation distribution and interpretation of the Mössbauer Fe^{2+} components in dioctahedral trans-vacant micas. *European Journal of Mineralogy*, **16**, 451–468.

Dainyak, L., Zviagina, B., Rusakov, V and Drits, V. 2006. Interpretation of the nontronite-dehydroxylate Mössbauer spectrum using EFG calculations. *European Journal of Mineralogy*, **18**, 753–764.

DeGrave, E., Vandenbruwaene, J. and van Bockstael, M. 1987 ^{57}Fe Mössbauer spectroscopic analysis of chlorite. *Physics and Chemistry of Minerals*, **15**, 173–180.

Doniach, S. and Sunjic, M. 1970. Many-electron singularity in X-ray photoemission and X-ray line spectra from metals. *Journal of Physics C: Solid State Physics*, **3**, 285–291.

Drits, V., Dainyak, G., Mulle,r F., Besson, G. and Manceaut, A. 1997. Isomorphous cation distribution in celadonites, glauconites and Fe-illites determined by infrared, Mössbauer and Exafs spectroscopies. *Clay Minerals*, **32**, 153–179.

Drits, V., McCarty, D. and Zviagina, B. 2006. Crystal-chemical factors responsible for the distribution of octahedral cations over trans- and cis-sites in dioctahedral 2:1 layer silicates. *Clays and Clay Minerals*, **54**, 131–152.

Drits, V., Zviagina, B., McCarty, D. and Salyn, A. 2010. Factors responsible for crystal-chemical variations in the solid solutions from illite to aluminoceladonite and from glauconite to celadonite. *American Mineralogist*, **95**, 348–361.

Dyar, M.D. 1984 Precision and interlabolatory reproducibility of measurments of the Mössbauer effect in minerals. *American Mineralogist*, **69**, 1127–1144.

Dyar, M.D. 2002. Optical and Mössbauer Spectroscopy of Iron in Micas. *Reviews in Mineralogy and Geochemistry*, **46 (1)**, 313–349.

Dyar, M.D., Agresti, D., Schaefer, M., Grant, C. and Sklute, E. 2006. Mössbauer spectroscopy of earth and planetary materials. *Annual Review of Earth and Planetary Sciences*, **34 (1)**, 83–125.

Elmi, C., Brigatti, M., Guggenheim, S., Pasquali, L., Montecchi, M. and Nannarone, S. 2014 Crystal chemistry and surface configurations of two polylithionite-1M crystals. *American Mineralogist*, **99**, 2049–2059.

Elmi, C., Guggenheim, S. and Gier R. 2016. Surface crystal chemistry of phyllosilicates using X-Ray photoelectron spectroscopy: A Review. *Clays and Clay Minerals*, **64**, 537–551.

Farmer, V. 1974. The layered silicates In: Farmer, V.C. (Ed.), The infrared spectra of minerals, 331–363. The Mineralogical Society Monograph 4; London.

Foster, M. 1960. Layer charge relations in the dioctahedral and trioctahedral micas. *American Mineralogist*, **45**, 383–398.

Gates, W. 2005. Infrared spectroscopy and the chemistry of dioctahedral smectites. In: Klopproge, J.T. (Ed.), The Application of Vibrational Spectroscopy to Clay Minerals and Layered Double Hydroxides, CMS Workshop Lectures, vol. 13, 125–168. The Clay Mineral Society; Aurora, CO.

Gates, W. 2008. Cation Mass-valence sum (CM-VS) approach to assigning OH – bending bands in dioctahedral smectites. *Clays and Clay Minerals*, **56**, 10–22.

Goodman, B. 1976. The Mössbauer spectrum of a ferrian muscovite and its implications in the assignment of sites in dioctahedral micas. *Mineralogical Magazine*, **40**, 513–517.

Heller-Kallai, L. and Rozenson. I. 1981. The use of Mössbauer spectroscopy of iron in clay mineralogy. *Physics and Chemistry of Minerals*, **7**, 223–238.

Hesse, J. and Riibartsch, A. 1974. Model independent evaluation of overlapped Mössbauer spectra. *Journal of Physics E: Scientific Instruments*, **7**, 526–532.

Ihekweme, G., Shondo, J., Orisekeh, K., Kalu-Uka, G., Chukwujike Nwuzor, I. and Onwualu, P. 2020. Characterization of certain Nigerian clay minerals for water purification and other industrial applications. *Heliyon*, **6**, e03783.

Kaky, K., Şakar, E., Akbaba, U., Kasapoğlu, A., Sayyed, M., Gür, E., Baki, S. and Mahdi, M. 2019. X-ray photoelectron spectroscopy (XPS) and gamma-ray shielding investigation of boro-silicate glasses contained alkali/alkaline modifier. *Results in Physics*, **14**, 102438.

Kloprogge, J. 2017. Raman spectroscopy of clay minerals. In: Gates, W.P., Kloprogge, J.T., Madejova, J. and Bergaya, F. (Eds), Infrared and Raman Spectroscopies of Clay Minerals, 150–199. Elsevier; Amsterdam.

Kloprogge, J. and Wood, B. 2018. X-ray photoelectron spectroscopy and Raman microscopy of a ferroan platinum crystal from the Kondyor Massif, Russian Far East. *Spectroscopy Letters*, **21**, 43–48.

Li, G., Peacor, D., Coombs, D. and Kawachi, Y. 1997. Solid solution in the celadonite family: the new minerals ferroceladonite, $K_2Fe^{2+}Fe^{3+}Si_8O_{20}(OH)_4$, and ferroaluminoceladonite, $K_2Fe^{2+}Al_2Si_8O_{20}(OH)_4$. *American Mineralogist*, **82**, 503–511.

Li, H., Zhang, L. and Christy, A. 2011. The correlation between Raman spectra and the mineral composition of muscovite and phengite. In: Dobrzhinetskaya, L.F., Faryad, S.W., Wallis, S. and Cuthbert, S. (Eds), Ultrahigh-Pressure Metamorphism, 187–212. Elsevier; Amsterdam.

Liu, Z. and Brown, N. 1998. XPS characterization of mica surfaces processed using a radio-frequency (rf) argon plasma. *Journal of Physics D: Applied Physics*, **31**, 1771–1781.

Loh, E. 1973. Optical vibrations in sheet silicates. *Journal of Physics C: Solid State Physics*, **6**, 1091–1104.

Madejová, J., Gates, W. and Petit, S. 2017. IR spectra of clay minerals. In: Gates, W.P., Kloprogge, J.T., Madejova, J. and Bergaya, F. (Eds), Infrared and Raman Spectroscopies of Clay Minerals, 107–149. Elsevier; Amsterdam.

Marco-Brown, J., Gaigneaux, E., Torres Sánchez, R. and Santos Afonso, M. 2019. Adsorption of picloram on clays nontronite, illite and kaolinite: equilibrium and herbicide-clays surface complexes. *Journal of Environmental Science and Health B*, **54**, 281–289.

Martínez-Alonso, S., Rustad, J. and Goetz, A. 2002. Ab initio quantum mechanical modeling of infrared vibrational frequencies of the OH group in dioctahedral phyllosilicates. Part II: main physical factors governing the OH vibrations. *American Mineralogist*, **87**, 1224–1234.

McKeown, D., Bell, M. and Etz, E. 1999. Vibrational analysis of the dioctahedral mica: 2M1 muscovite. *American Mineralogist*, **84**, 1041–1048.

Michalski, J., Poulet, F., Bibring, J. and Mangold, N. 2010. Analysis of phyllosilicate deposits in the Nili Fossae region of Mars: comparison of TES and OMEGA data. *Icarus*, **20**, 269–289.

Mineeva, R. 1978. Relationship between Mössbauer spectra and defect structure in biotites from electric field gradient calculations. *Physics and Chemistry of Minerals*, **2**, 267–277.

Muller, F., Drits, V., Plancon, V. and Robert, J.-L. 2000. Structural transformation of 2:1 dioctahedral layer silicates during dehydroxylation-rehydroxylation reactions. *Clays and Clay Minerals*, **48 (5)**, 572–585.

Ospitali, F., Bersani, D., Lonardo, G. and Lottici, P. 2008. "Green earths": vibrational and elemental characterization of glauconites, celadonites and historical pigments. *Journal of Raman Spectroscopy*, **39**, 1066–1073.

Petit, S. 2005. Crystal-chemistry of talcs: A NIR and MIR spectroscopic approach. In: Klopproge, J.T. (Ed.), The Application of Vibrational Spectroscopy to Clay Minerals and Layered Double Hydroxides, CMS Workshop Lectures, 41–64. The Clay Mineral Society, 13; Aurora, CO.

Rancourt, D. 1994. Mössbauer spectroscopy of minerals II. Problem of resolving cis and trans octahedral Fe^{2+} sites. *Physics and Chemistry of Minerals*, **21**, 250–257.

Rancourt, D., McDonald, A., Lalonde, A. and Ping J. 1993. Mössbauer absorber thicknesse for accurate site populations in Fe-bearing minerals. *American Mineralogist*, **78**, 1–7.

Redhammer, G., Amthauer, G., Lottermoser, W., Bernroider, M., Tippelt, G. and Roth, G. 2005. X-ray powder diffraction and ^{57}Fe Mössbauer spectroscopy of synthetic trioctahedral micas $\{K\}[Me_3](TSi_3)O_{10}(OH)_2$, Me = Ni^{2+}, Mg^{2+}, Co^{2+}, Fe^{2+}; T = Al^{3+}, Fe^{3+}. *Mineralogy and Petrology*, **85**, 89–115.

Redhammer, G., Beran, A., Schneider, J., Amthauer, G. and Lottermoser, W. 2000. Spectroscopic and structural properties of synthetic micas on the annite-siderophyllite binary: Synthesis, crystal structure refinement, Mössbauer, and infrared spectroscopy. *American Mineralogist*, **85**, 449–465.

Richardson, S. and Richardson, J. 1982. Crystal structure of a pink muscovite from archer's post, Kenya: implications for reverse pleochroism in dioctahedral micas. *American Mineralogist*, **67**, 69–75.

Rieder, M., Cavazzini, G., D'Yakonov, Y., Frank-Kameneckii, V., Gottardi, G., Geggenheim S., Koval, P., Müller, G., Neiva, A., Radoslovich, E., Robert, J., Sassi, F., Takeda, H., Weiss, Z. and Wones, D. 1998. Nomenclature of the micas. *Canadian Mineralogist*, **36**, 905–912.

Rinaudo, C., Roz, M., Boero, V. and Franchini-Angela, M. 2004. FT-Raman spectroscopy on several di- and trioctahedral T-O-T phyllosilicates. *Neues Jahrbuch für Mineralogie-Monatshefte*, **12**, 537–554.

Robert J. and Kodama, H. 1988. Generalization of the correlations between hydroxyl-stretching wave numbers and com-

position of micas in the system $K_2O_aMgO_aAl_2O_{3a}SiO_{2a}H_2O$: a single model for trioctahedral and dioctahedral micas. *American Journal of Science*, **288A**, 196–212.

Russell, J. and Fraser, A. 1994. Infrared methods. In: Wilson, M.J. (Ed.), Clay mineralogy: Spectroscopic and Chemical Determinative Methods, 11–67. Chapman & Hall; London.

Schingaro, E., Lacalamita, M., Scordari, F. and Mesto, E. 2013. 3T-phlogopite from Kasenyi kamafugite (SW Uganda): EPMA, XPS, FTIR, and SCXRD study. *American Mineralogist*, **98**, 709–717.

Schroeder, P. 1990. Far infrared, X-ray diffraction and chemical investigation of potassium micas. *American Mineralogist*, **75**, 983–991.

Schuttlefield, J., Cox, D. and Grassian, V. 2007. An investigation of water uptake on clays minerals using ATR-FTIR spectroscopy coupled with quartz crystal microbalance measurements. *Journal of Geophysical Research*, **112**, D21303.

Seyama, H. and Soma, M. 1985. Bonding-state characterization of the constitutent elements of silicate minerals by X-ray photoelectron spectroscopy. *Journal of the Chemical Society, Faraday Transactions*, **81 (2)**, 485–495.

Süzer, Ş., Ertaş, N. and Ataman, O. 1999. XPS Characterization of Bi and Mn Collected on Atom-Trapping Silica for AAS. *Applied Spectroscopy*, **53 (4)**, 479–482.

Środoń, J. 1999. Nature of mixed-layer clays and mechanisms of their formation and alteration. *Annual Review of Earth and Planetary Sciences*, **27**, 19–53.

Tischendorf, G., Forster, H., Gottesmann B. and Rieder, M. 2007. True and brittle micas: composition and solid-solution series. *Mineralogical Magazine*, **71 (3)**, 285–320.

Tissot, H., Li, L., Shaikhutdinov, S. and Freund, H. 2016. Preparation and structure of Fe-containing aluminosilicate thin films. *Physical Chemistry Chemical Physics*, **18**, 25027–25035.

Tlili, A., Smith, D., Beny, J. and Boyer, H. 1989. A Raman microprobe study of natural micas. *Mineralogical Magazine*, **53**, 165–179.

Tsipursky, S. and Drits, V. 1984. The distribution of octahedral cations in the 2:1 layers ofdioctahedral smectites studied by oblique-texture electron diffraction. *Clay Minerals*, **19**, 177–193.

Vantelon, D., Belkhou, R., Bihannic, I., Michot, L., Montargès-Pelletier, E. and Robert, J. 2009. An XPEEM study of structural cation distribution in swelling clays. I. Synthetic trioctahedral smectites. *Physics and Chemistry of Minerals*, **36**, 593–602.

Velde, B. 1983. Infrared OH-stretch bands in potassic micas, talcs and saponites; influence of electronic configuration and site of charge compensation. *American Mineralogist*, **68**, 1169–1173.

Zviagina, B., Drits, V., Rodoń, J., McCarty, D. and Dorzhieva, O. 2015. The illite-aluminoceladonite series: distinguishing features and identification criteria from X-ray diffraction and infrared spectroscopy data. *Clays and Clay Minerals*, **63 (5)**, 378–394.

Zviagina, B., McCarty, D., Rodoń, J. and Drits, V. 2004. Interpretation of infrared spectra of dioctahedral smectites in the region of oh-stretching vibrations. *Clays and Clay Minerals*, **52 (4)**, 399–410.

Zviagina, B., Sakharov, B. and Drits, V. 2007. X-ray diffraction criteria for the identification of trans- and cis-vacant varieties of dioctahedral micas. *Clays and Clay Minerals*, **55 (5)**, 467–480.

Manuscript submitted: 26th November 2021
Revised version accepted: 14th June 2022